Statistical independence of the initial conditions in chaotic mixing

J. M. García de la Cruz* and J. C. Vassilicos
Imperial College London, South Kensington Campus, London SW7 2AZ, United Kingdom

L. Rossi
CEA, Paris-Saclay University, Den-STMF, Gif-sur Yvette F-91191, France

(Received 12 January 2017; published 17 November 2017)

Experimental evidence of the scalar convergence towards a *global strange eigenmode* independent of the scalar initial condition in chaotic mixing is provided. This convergence, underpinning the independent nature of chaotic mixing in any passive scalar, is presented by scalar fields with different initial conditions casting statistically similar shapes when advected by periodic unsteady flows. As the scalar patterns converge towards a *global strange eigenmode*, the scalar filaments, locally aligned with the direction of maximum stretching, as described by the Lagrangian stretching theory, stack together in an inhomogeneous pattern at distances smaller than their asymptotic minimum widths. The scalar variance decay becomes then exponential and independent of the scalar diffusivity or initial condition. In this work, mixing is achieved by advecting the scalar using a set of laminar flows with unsteady periodic topology. These flows, that resemble the tendril-whorl map, are obtained by morphing the forcing geometry in an electromagnetic free surface 2D mixing experiment. This forcing generates a velocity field which periodically switches between two concentric hyperbolic and elliptic stagnation points. In agreement with previous literature, the velocity fields obtained produce a chaotic mixer with two regions: a central mixing and an external extensional area. These two regions are interconnected through two pairs of fluid conduits which transfer clean and dyed fluid from the extensional area towards the mixing region and a homogenized mixture from the mixing area towards the extensional region.

DOI: 10.1103/PhysRevE.96.052212

I. INTRODUCTION

Mixing of a passive scalar, θ, in a domain, $\mathbf{r}$, can be described by the transport equation

$$\frac{\partial\theta(\mathbf{r},t)}{\partial t} = \mathcal{P}\theta(\mathbf{r},t) := [\kappa\Delta - \mathbf{u}(\mathbf{r},t)\cdot\nabla]\theta(\mathbf{r},t), \qquad (1)$$

where the linear advective-diffusive operator, $\mathcal{P}$, depends on the diffusivity, κ, and, through the velocity field, $\mathbf{u}$, on time, t. In a time-periodic system of period T, using a Fourier spatial and Floquet temporal transformation, a scalar field in the wave-number domain at time, t can be mapped into a new scalar field at time $t+T$ as $\hat{\theta}^{t+T} = \hat{\mathcal{P}}\hat{\theta}^{t}$. The Frobenius-Perron operator $\hat{\mathcal{P}}$ can be truncated for those elements associated with wave numbers $\lambda_B \ll \sqrt{s/\kappa}$, defined by the flow stretching rate, s [1–3]. As in analytical examples (such as the homogeneous baker [4] or Arnold's cat maps [5]), the advective term in $\hat{\mathcal{P}}$ can be ideally designed so as to transfer all the scalar content in any wave number to a higher one, leading to a superexponential variance decay for any finite diffusivity. In general, however, advection disperses the scalar across a range of length scales, some of them larger than the original one, generating small- and large-scale persistent scalar patterns. These patterns are defined by the eigenmodes of $\hat{\mathcal{P}}$ with the largest eigenvalues [6–8], and, in the limit $\mathrm{Pe} \gg 1$ (where the Péclet number, Pe, is the ratio between advective and diffusive transport rates), lead to an exponential variance decay independent of the diffusivity. Such homogenization slowdown has been attributed to two competing phenomena acting at local and global spatial scales and respectively controlling the variance decay when the scalar length scale is much smaller or similar to the flow length scale [9,10]. At local length scales, the Lagrangian stretching theory predicts that the long-term variance decay rate is controlled by those scalar gradients misaligned with the direction perpendicular to the locally fastest growing particle separation [11]: As the exponentially elongating scalar thinnest filaments align with the local stretching direction, they reach a minimum width, known as Batchelor length scale, $\ell_B = 1/\lambda_B = \sqrt{\kappa/s}$, [12], so the scalar variance decay becomes only a function of the filament elongation.

At a global length scale, inhomogeneous advection stacks scalar layers nonuniformly in the domain, curbing the variance decay as the distance between layers becomes smaller than ℓ_B. A global eigenmode, independent of the scalar, is then distinguishable [2,3,8,13]. Since the existence of the *strange eigenmode* was postulated [14], theoretical, numerical, and experimental works have evidenced its presence, showing how periodic flows rearrange passive scalars in temporal recurrent patterns in close [1,15–20] or open flows [21,22]. A *global strange eigenmode* nevertheless implies a stronger convergence: The eigenmodes of $\hat{\mathcal{P}}$ should exclusively depend on the velocity field, and different initial conditions should cast the same temporal recurring pattern, statistically mixing in a similar fashion. This paper evidences how periodic flows impose on the scalar mixed recurring temporal patterns independent of the scalar initial condition. This independence on initial conditions is explicitly demonstrated in our experimental configuration. As expected, variance decay under the presence of these patterns becomes exponential.

Most of the experimental work concerned with the *strange eigenmode* to date has used either electromagnetic alternating

*marcos@imperial.ac.uk

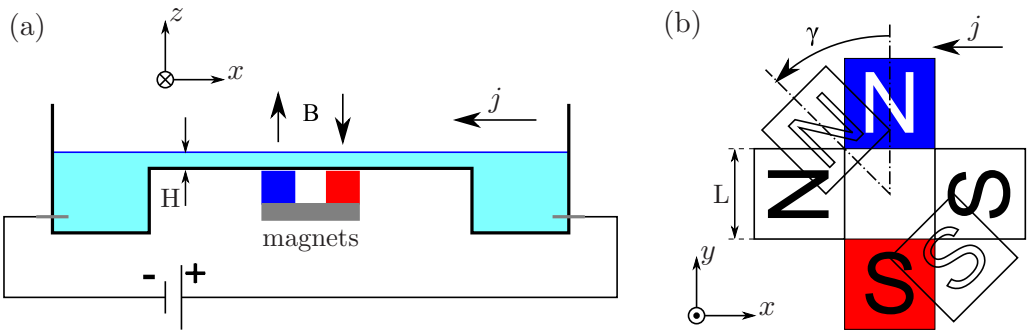

FIG. 1. Electromagnetic tank and magnet positioning. (a) Layout of the experimental setup with magnetic field B and current j. (b) Magnet positioning with angle γ. Reference system: $\mathbf{r} = (x,y,z)$.

forcing with constant magnetic topology, which relies on inertia to produce irreversibility [16–20], or friction forces in cavity flows [23] or eggbeaters [21,22]. This research used electromagnetic forced flows with morphing forcing topology. Mixing then occurred within a velocity field similar to the tendril-whorl map (TWM) [24,25], which consists of a periodic switch between the steady flows generated by concentric hyperbolic or elliptic stagnation points. Such forcing has the practical advantage that it can generate chaotic advection in a Stokes flow. Also, the similitude with the TWM provides a reference for the analysis of the velocity fields, as well as an experimental demonstration of previous theoretical results.

This paper is outlined as follows. The experimental details are described in Sec. II. Section III presents and discusses the results before conclusions are made in Sec. IV.

II. APPARATUS AND EXPERIMENTAL PROCEDURE

A. Laboratory apparatus

A shallow two-layer stratified solution of NaCl, of total depth $H = 6$ mm, was electromagnetically forced, as conceived in [26], using the setup sketched in Fig. 1(a).

The magnetic field is generated by a pair of cubic magnets of edge 40 mm with a magnetic strength of $B = 0.3$ T, placed $L = 40$ mm apart. The angle γ [Fig. 1(b)] defines the magnet attitude and was switched between 0° and 90° at a speed of $\pi/2$ rad s^{-1}. The electric field, generated by two arrays of 20 platinum electrodes equispaced 20 mm apart, produces a nominal current of 24 mA, with a standard deviation smaller than 0.5%.

A central square of side 440 mm is recorded by a 2048 × 2048-pixel camera (1 pix ≈ 0.21 mm). The brine free surface extends up to a square of side 600 mm. The 1-mm-thick bottom wall is in contact with the magnets and has a maximum flatness error of 0.4 mm.

B. Velocity field acquisition

Particle image velocimetry (PIV) was employed to acquire the velocity field, using floating particles of Pliolite DF01 (≈150 μm) and an in-house PIV software with numerical uncertainty $\epsilon \approx 0.05$ pix frame^{-1} [27]. The PIV mesh is a regular array of 222 × 222 points covering a square of about 380 mm per side. A 3 × 3 smoothing filter was applied over the velocity fields. Virtual particles were tracked in the velocity fields acquired using an adaptive step-size fourth-order Runge-Kutta method [28] validated in [29]. The velocity fields at each time step were evaluated using a third-degree polynomial interpolation in time and space. To avoid the loss of the virtual particles, the velocity field orbits were numerically closed outside the PIV area and up to a square of size 600 mm, assuming a 2D Stokes flow and employing impermeable and nonslip boundary conditions in the domain edge and the acquired velocity field in the PIV border [29]. The velocity field stagnation points were found using the Poincaré index of small orbits [30,31].

C. Scalar field acquisition

A rhodamine 6G (Rh6G) solution (1 ml) was injected over a two-layer stratified brine of 0.5 mm of fresh water over 5.5 mm of a solution of NaCl in water at 80 g l^{-1} [29], leaving a blob of dye of around 40 mm diameter and 0.8 mm depth. Laser-induced florescence was employed to acquire each i scalar field, $\theta^i(\mathbf{r},t)$. A 532-nm, 200-mJ Nd:YAG laser expanded into a cone excited the Rh6G. A 540-nm-long pass filter blocked the laser light while allowing the light emitted by the Rh6G, with wavelength emission peak at 552 nm, to reach the camera CCD. Statistical convergence analysis showed that the 31 initial conditions positioned as in Fig. 2(a) led to an error in the results smaller than 4% with 95% certainty. Positions symmetric with respect to the rig center were deliberately avoided. To consider scalar initial conditions with different scales, and based on the linearity of the transport operator, the combination of all the samples was used as an additional initial condition, the combined initial condition, as presented in Fig. 2(b).

At the low Rh6G concentration, $c \approx 2 \times 10^{-5}$ M, employed, the dye fluorescence is proportional to c and the exciting laser intensity, I_0 [32]. The spatial inhomogeneity in I_0 was calibrated by acquiring the light emitted by several depths of a homogeneous concentration of Rh6G and fitting, for every pixel, a linear regression between the light intensity and the depth of reference Rh6G [33]. This is equivalent to a 2D concentration field which, except for errors associated with vertical velocity gradients and gravity currents induced by the dye injection, follows a 2D advection-diffusion process [33].

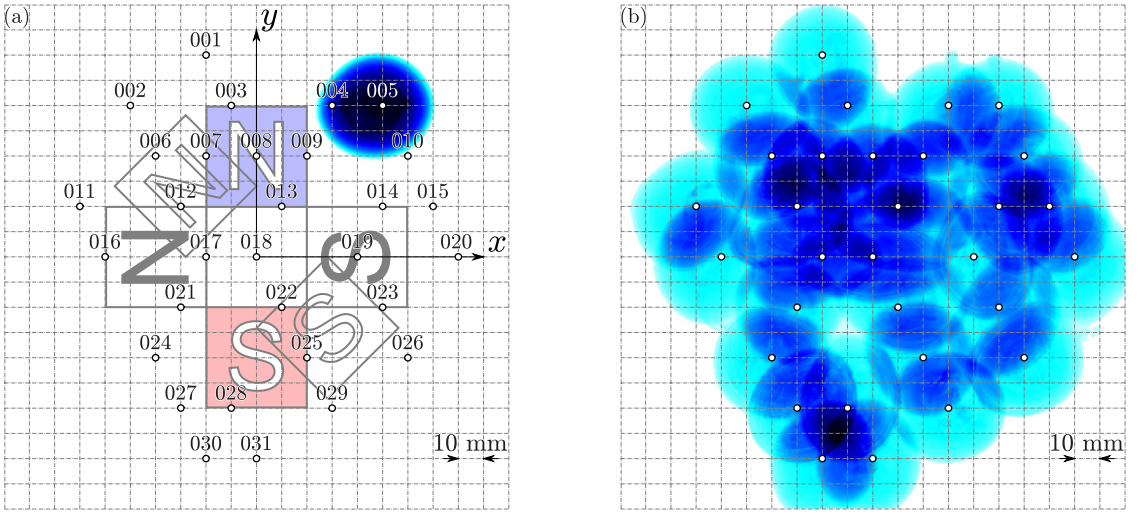

FIG. 2. Scalar initial conditions. (a) Centers of the scalar blob initial positions, labeled with their numbers, over magnets, with "blob 05" presented as an example. (b) Combined initial condition.

To reduce the effect of noise, the scalar variance and mean gradient squared were computed as the spatial average of the cross product between two pictures 100 ms apart [33]. The scalar fields presented are the average of such two consecutive pictures. These averaged scalar fields are also employed in the concentration correlations between samples.

Operators $\langle\eta\rangle$ and $\overline{\eta}$ respectively indicate spatial and intersample average of the variable η. The operator $\langle\eta,\zeta\rangle$ expresses the correlation (Pearson's coefficient) between the variables η and ζ, defined as $\langle\eta,\zeta\rangle = \langle\eta'\zeta'\rangle/\sqrt{\langle\eta'^2\rangle\langle\zeta'^2\rangle}$, where $\eta' = \eta - \langle\eta\rangle$.

III. RESULTS

A. Description of the velocity field

The flows obtained with the magnet angles $\gamma = 90^\circ$ and $\gamma = 0^\circ$ are steady [30]: The root mean square (rms) of their velocity temporal standard deviation is smaller than 5% of their velocity rms, U_{rms}, measured in a central circular area of 100 mm radius. The velocity fields employed, $\mathbf{u}_\gamma$, are presented in Fig. 3, for which $\text{Re}_H = U_{\text{rms}}H/\nu \approx 30$, $\text{Re}_L = U_{\text{rms}}L/\nu \approx 200$, and $\text{Pe}_L = U_{\text{rms}}L/\kappa \approx 2\times10^6$, where $\nu \approx 1$ mm^2 s^{-1} is the water viscosity and $\kappa \approx 10^{-4}$ mm^2 s^{-1} is the diffusivity of Rh6G in water [34].

The flow in Fig. 3(a), $\mathbf{u}_{90^\circ}$, presents a main central elliptic stagnation point (ESP) and two other weaker ESPs around $\pm(75,15)$ mm. The flow in Fig. 3(b), $\mathbf{u}_{0^\circ}$, presents a main central hyperbolic stagnation point (HSP) and four other ESPs around $(\pm30, \pm 30)$ mm.

In both cases, a scalar sized with the magnet length and randomly released within 100 mm of the magnet center, as shown in Fig. 2(a), has a turnover time between 30 and 80 s, with a probability larger than 95% [29]. Based on this, the periods, T, of the magnet switching, 50, 100, and 200 s, were selected as twice the time for each steady velocity field to either never complete a turnover time (25 s), complete a turnover

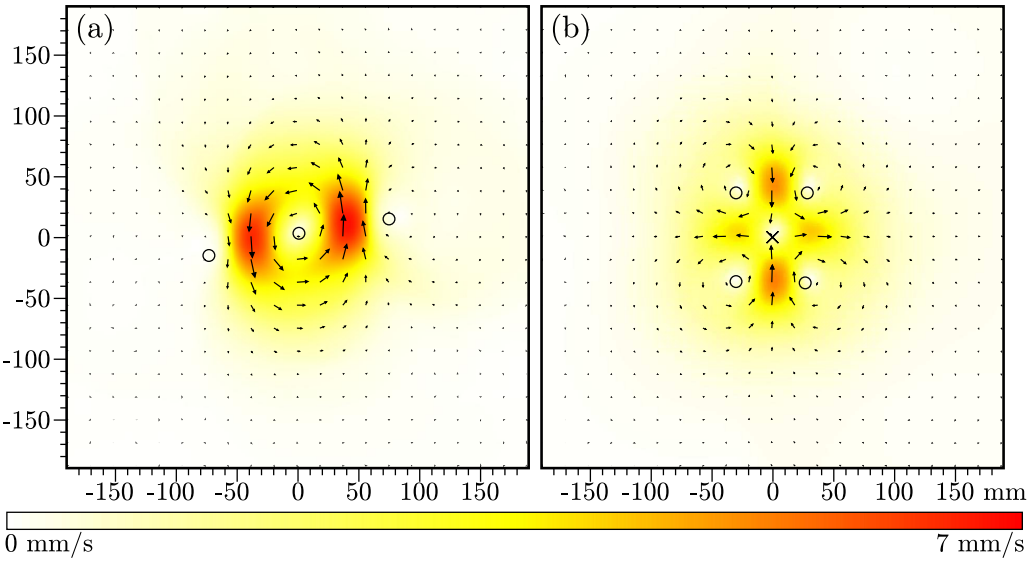

FIG. 3. Steady velocity fields obtained using (a) $\gamma = 90^\circ$ and (b) $\gamma = 0^\circ$. $\times$ = HPS and $\circ$ = ESP.

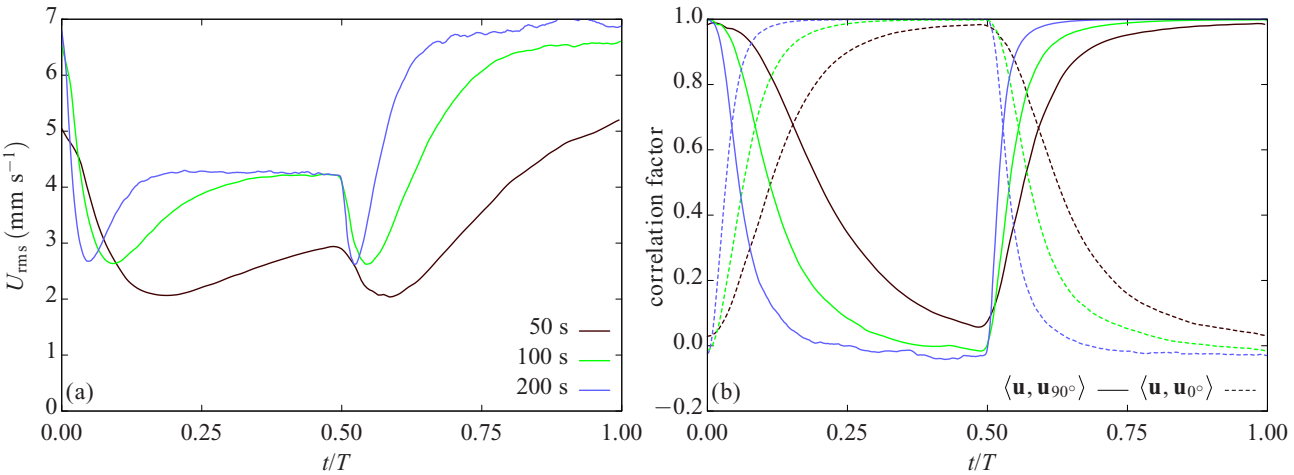

FIG. 4. Velocity field statistics of the flows considered: (a) $U_{\rm rms}$ in a central domain of radius 100 mm and (b) velocity correlation with the steady flows presented in Fig. 3(b). The magnets are switched from $\gamma = 90^\circ$ to $\gamma = 0^\circ$ at $t/T = 0$ and from $\gamma = 90^\circ$ to $\gamma = 0^\circ$ at $t/T = 0.5$.

time for about half of the initial conditions (50 s), or always complete a turnover time (100 s).

The evolution of the velocity fields obtained by periodic magnetic switching is summarized in Fig. 4 through the velocity root mean squared, $U_{\rm rms}$, and the velocity correlation, $\langle \mathbf{u}, \mathbf{u}_\gamma \rangle$, with the steady velocity fields, $\mathbf{u}_\gamma$, presented in Fig. 3.

At low Re_H, the transient of the velocity field deficit scales with the exponential of the fluid kinematic viscosity and the square of the fluid thickness, which, for this setup, has a typical time scale between 30 and 40 s. Therefore, as presented, the 50-s-period flow never reaches a steady state, neither in intensity nor in direction, whereas, for the 200-s-period flow, the transient represents a small part of the cycle.

After the magnet switch from $\gamma = 90^\circ$ to $\gamma = 0^\circ$, the central ESP splits into two ESPs and one HSP [35]. The HSP remains in the rig center, while the two new ESPs respectively travel towards the positions $\pm(30,30)$ mm and the two secondary lateral ESPs of the flow travel towards the positions $\pm(-30,30)$ mm. This process is reversed for the magnet switch from from $\gamma = 0^\circ$ to $\gamma = 90^\circ$, as summarized in Figs. 5 and 6.

Figure 5 presents the position of the HSP and ESP during one forcing cycle. The position of the stagnation points defines the topology of the velocity fields. As observed, the evolution of the flow topology during one cycle in the 50-s-period configuration is similar to those of the other two cases. Figure 6 presents the temporal evolution of the flow stagnation points. This figure highlights how the topological transients (i.e., the position of the stagnation points) are less relevant than the geometrical transients (i.e., the flow velocity and correlation with the baseline flows): In all three cases, a central HSP alternates in time with a central ESP, as intended to simulate the TWM. Since a quantitative comparison between the mixing properties of the three configurations is not intended, the geometrical difference between the cases should not affect the discussion.

A summary of the stirring properties of the flows is presented in Fig. 7, obtained by virtually tracking during one

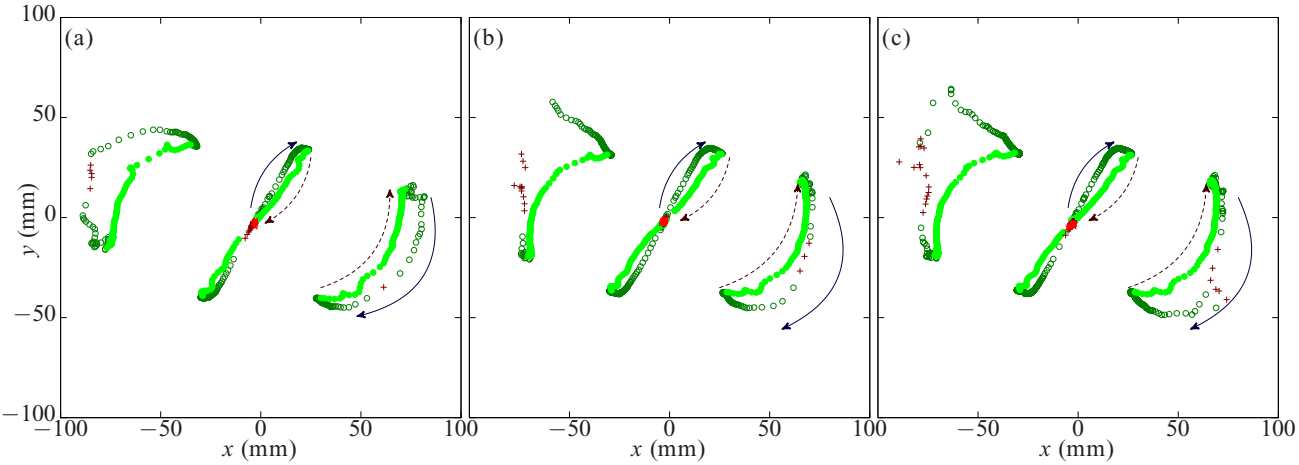

FIG. 5. Stagnation points of the velocity fields in one cycle using (a) $T = 50$ s, (b) $T = 100$ s, and (c) $T = 200$ s. Elliptic ($0 - T/2$, ○; $T/2 - T$, ●) and hyperbolic ($0 - T/2$, +; $T/2 - T$, ×) stagnation points and the direction that they follow ($0 - T/2$, ⟶; $T/2 - T$, ⟶) during one forcing cycle.

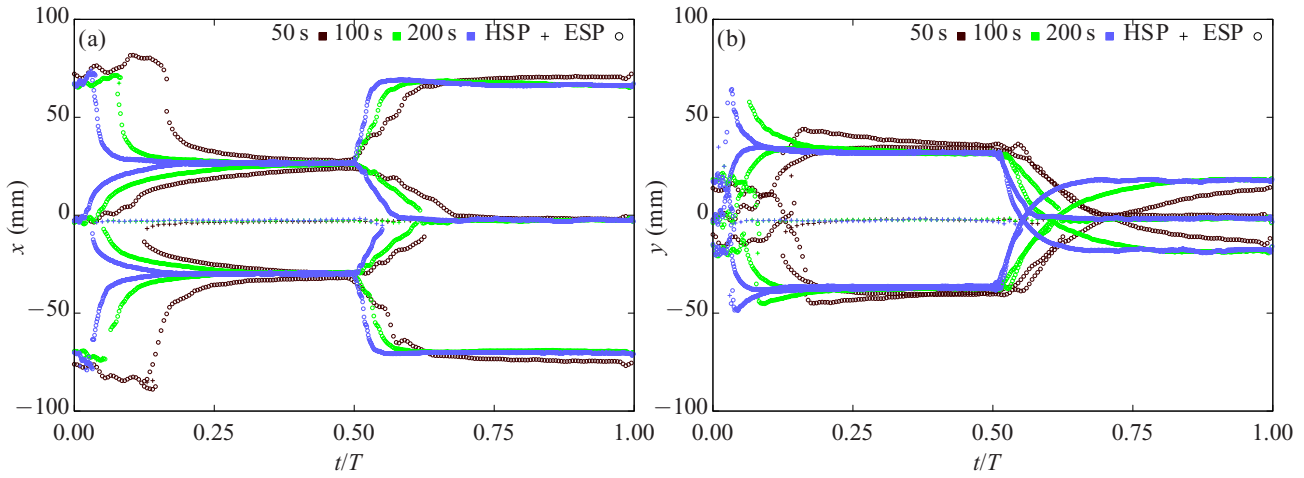

FIG. 6. Stagnation points in one cycle of the unsteady velocity fields. (a) Temporal evolution of x (a) and y (b) position of the elliptic (ESP) and hyperbolic (HSP) stagnation points. The magnets are switched from $\gamma = 90^\circ$ to $\gamma = 0^\circ$ at $t/T = 0$ and from $\gamma = 90^\circ$ to $\gamma = 0^\circ$ at $t/T = 0.5$.

forcing period 128 × 128 particles covering the rig. This figure shows the period-1 Poincaré maps plotted over color maps presenting the average increment during one forcing period of the distance between one particle and its eight adjoining neighbors and normalized with the total distance traveled by that particle. This last measure is qualitatively similar to the finite time Lyapunov exponents [11] and quantifies the impact on the particle path of small variations on the initial conditions. Two squares demarcate the camera viewing area (CAM) and the limits of the PIV mesh considered (outside which the flow was simulated, not measured).

As observed, the central part of the flows presented in Fig. 7 contains a mixing area where particles quickly move away from their neighbors. In agreement with [25], this mixing area increases its size with the flow period. In the three cases, the fluid in an intermediate extensional area leaves and reenters into the mixing region through two pairs of conduits, similar to those observed in the TWM around the outer period-1 periodic points [25]. These conduits connect the extensional and mixing regions and form a unique inhomogeneous chaotic area. The dashed circles in Fig. 7, whose radii are summarized in Table I, delimit mixing and extensional regions for each configuration. Delimiting this chaotic area there is a mixing barrier separating the outer recirculating flow. The chaotic area appears to shrink for larger forcing periods.

B. Scalar statistics

Most of the stretching and folding happens in the mixing area, continuously fed with clean and dyed fluid coming from the extensional region, towards which a more homogeneous mixture is expelled. This is equivalent to a highly inhomogeneous baker map, whose major region suffers only a mild stretching while all the stirring is confined to a smaller area, still being fully chaotic. For time scales much shorter than the recirculation period in the extensional region, T_S, the map,

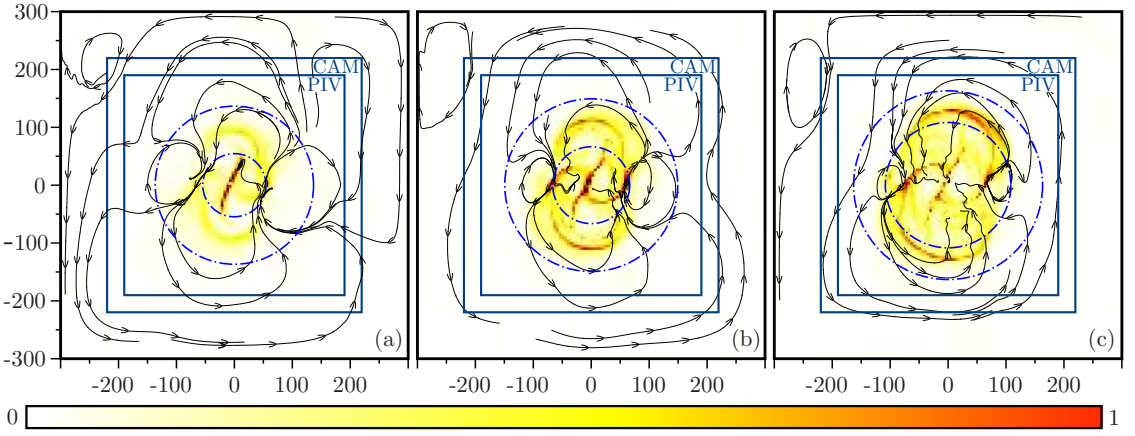

FIG. 7. Poincaré maps and relative particle dispersion, obtained as the increment on the average distance between one particle and its eight neighbors during one forcing period, normalized with the distance traveled by that particle (fields obtained tracking a 128 × 128 grid of particles) for forcing periods (a) 50 s, (b) 100 s, and (c) 200 s. The camera (CAM) and PIV areas are highlighted. The dash-dotted circles delimit mixing and extensional regions for each configuration.

nevertheless, behaves as an open baker map [21]. If evidence of a *global strange eigenmode* is to be found for $t \ll T_S$, this central region should be identified, since the evolution of the extensional region is much slower than one period and would only spuriously increase the spatial correlation, regardless of the existence of recurrent patterns.

Figure 8 presents an overview of the stirring generated by the flows on the scalar. For each flow configuration ($T = 50$ s, $T = 100$ s, and $T = 200$ s), snapshots of the patterns arrived at by one arbitrary initial position and the combined initial condition are presented at times t/T: 0, 1, 2, 3, and 4. In all cases, the domain presented is the central square of side 440 mm, labeled as CAM in Fig. 7. The conduits connecting the extensional and mixing regions observed in the Poincaré maps can be identified in the scalar patterns, especially for the combined initial condition, as those channels feeding the mixing region with clean fluid and expelling mixed dye to the extensional region.

The central mixing areas in these flows, elongated in a diagonal as presented in Fig. 7, are again approximately delimited by the circumferences in Fig. 8: Outside the larger circumference there is no mixing region, whereas inside the smaller circumference there is only a mixing region. To find these limits, use was made of the expected high correlation between scalar patterns one forcing period apart within the mixing area, resulting from the recurrent patterns observed in chaotic mixing [15–22]. On the contrary, the correlation between patterns half a period apart is expected to be low in the mixing region, but high in the extensional area. A circular region of radius 220 mm centered in the rig was divided into 16 complementing concentric hoops of width 220 mm/16 = 13.75 mm. In each hoop, the spatial correlation (Pearson's coefficient) between scalar fields one period, $C_T^{\theta_i} = \langle \theta^i(\mathbf{r},t), \theta^i(\mathbf{r},t+T) \rangle$, and half a period, $C_{T/2}^{\theta_i}$, apart were compared for each scalar field, θ^i, and for the combined initial condition, $\overline{\theta^i}$.

Figure 9 presents the difference between the correlation one period and half a period apart for the combined initial condition ($C_T^{\overline{\theta_i}} - C_{T/2}^{\overline{\theta_i}}$) and the average of that difference for the rest of initial conditions ($\overline{C_T^{\theta_i} - C_{T/2}^{\theta_i}}$), averaged in time over the next-to-last cycle. In both cases, these values increase within the mixing region and drop as the hoops cover the extensional region. Negative values are reached when the hoops contain mostly an extensional region. The vertical lines in Fig. 9 show the radii selected as the limits between mixing, mixing-extensional, and extensional regions, summarized in Table I. These limits are consistent with the results presented in Fig. 7, in which the mixing area is characterized by a fast relative dispersion, and can also be visually verified in Fig. 8: At $t = 1T$ any initial condition will have spread all over the mixing region without entering the extensional area. Then, the outer limit should just cover all the dyed region, whereas the inner limit should be the largest not containing fresh fluid.

Along with the limits between mixing and extensional regions, Table I presents the temporal average over the next-to-last cycle of $\overline{C_T^{\theta_i}}$, $\overline{C_{T/2}^{\theta_i}}$, $C_T^{\overline{\theta_i}}$, and $C_{T/2}^{\overline{\theta_i}}$ calculated within a disk of size equal to each inner ring (only the mixing region). Correlations were performed at several length scales, $\mathcal{L}$, by successively considering the average concentration in groups of $2^n \times 2^n$ pixels (1 pix $\approx$ 0.21 mm), varying n from 0 to 6. The temporal evolution of $\overline{C_T^{\theta_i}}$ and $C_T^{\overline{\theta_i}}$ and its sensitivity to different length scales are presented in Fig. 10.

TABLE I. Region sizes. Radii delimiting the mixing and extensional regions and temporal average in the next-to-last cycle of the average of one period and half a period correlation samples, $\overline{C_T^{\theta_i}}$ and $\overline{C_{T/2}^{\theta_i}}$, or one period and half a period correlation of the combined initial position, $C_T^{\overline{\theta_i}}$ and $C_{T/2}^{\overline{\theta_i}}$, in a disk of radius equal to each inner ring (only covering mixing region in each case).

	Inner ring	Outer ring	Mixing region ($r < R_{\text{inner ring}}$)			
	(mm)	(mm)	$\overline{C_T^{\theta_i}}$	$\overline{C_{T/2}^{\theta_i}}$	$C_T^{\overline{\theta_i}}$	$C_{T/2}^{\overline{\theta_i}}$
$T = 50$ s	55	137.5	0.58	0.04	0.97	0.04
$T = 100$ s	68.75	151.25	0.49	0.02	0.95	0.03
$T = 200$ s	151.25	165	0.45	0.05	0.88	0.06

As shown in Fig. 10(a) both $\overline{C_T^{\theta_i}}$ and $C_T^{\overline{\theta_i}}$ start at a value near 0 and increase until, within 5 to 10 cycles, they oscillate with the flow period around a saturation limit, presented in Table I. In the $T = 200$ s case the experiment was interrupted before saturation. Noticeably, saturation for $C_T^{\overline{\theta_i}}$ in all configurations happens at higher values than for $\overline{C_T^{\theta_i}}$: While $C_T^{\overline{\theta_i}}$ average final values of the saturated cases are beyond 0.95, in line with previous literature [16], the cases $\overline{C_T^{\theta_i}}$ only reach values up to almost 0.6. This maximum correlation observed in $\overline{C_T^{\theta_i}}$ was attributed to two factors: low signal-to-noise ratio (SNR) and long-term strong inhomogeneities in the extensional region. On one hand, due to the small amount of dye used in each experiment, the signal of individual samples seems to be near the noise floor of the acquisition system. As more experiments, n, are averaged in a system with δ-correlated noise, the SNR increases as $\sqrt{n}$, with a total increase of around 5.5 for the entire set. On the other hand, strong inhomogeneities in the extensional region prevail for a time $T_S \gg T$ and affect the balance of scalar intensity within the mixing area. Both of these factors contributing to reduce $\overline{C_T^{\theta_i}}$ are palliated when the combined initial condition is considered in $C_T^{\overline{\theta_i}}$. The degree of spatial coherence in the scalar shapes required to reach the values achieved by $\overline{C_T^{\theta_i}}$ in this apparatus is highlighted by comparison with both $\overline{C_{T/2}^{\theta_i}}$ and $C_{T/2}^{\overline{\theta_i}}$ presented in Table I.

Figure 10(b) presents the temporal average over the next-to-last cycle of $\overline{C_T^{\theta_i}}$ and $C_T^{\overline{\theta_i}}$, against the minimum length scale, $\mathcal{L}$, employed. In all cases, the correlations nearly reach a flat slope at the minimum length scale considered, 1 pix $\approx$ 0.21 mm, which should be around the minimum scalar length scale of these regimes, ℓ_B, reached as the scalar filaments align with the local stretching direction. As a result, further camera resolutions should not significantly reduce the correlations or modify the results presented.

A closer view of the mixing region in the first quadrant is presented in Fig. 11 for the flow switching periods, T, 50, 100, and 200 s; for four initial conditions in each case (columns)

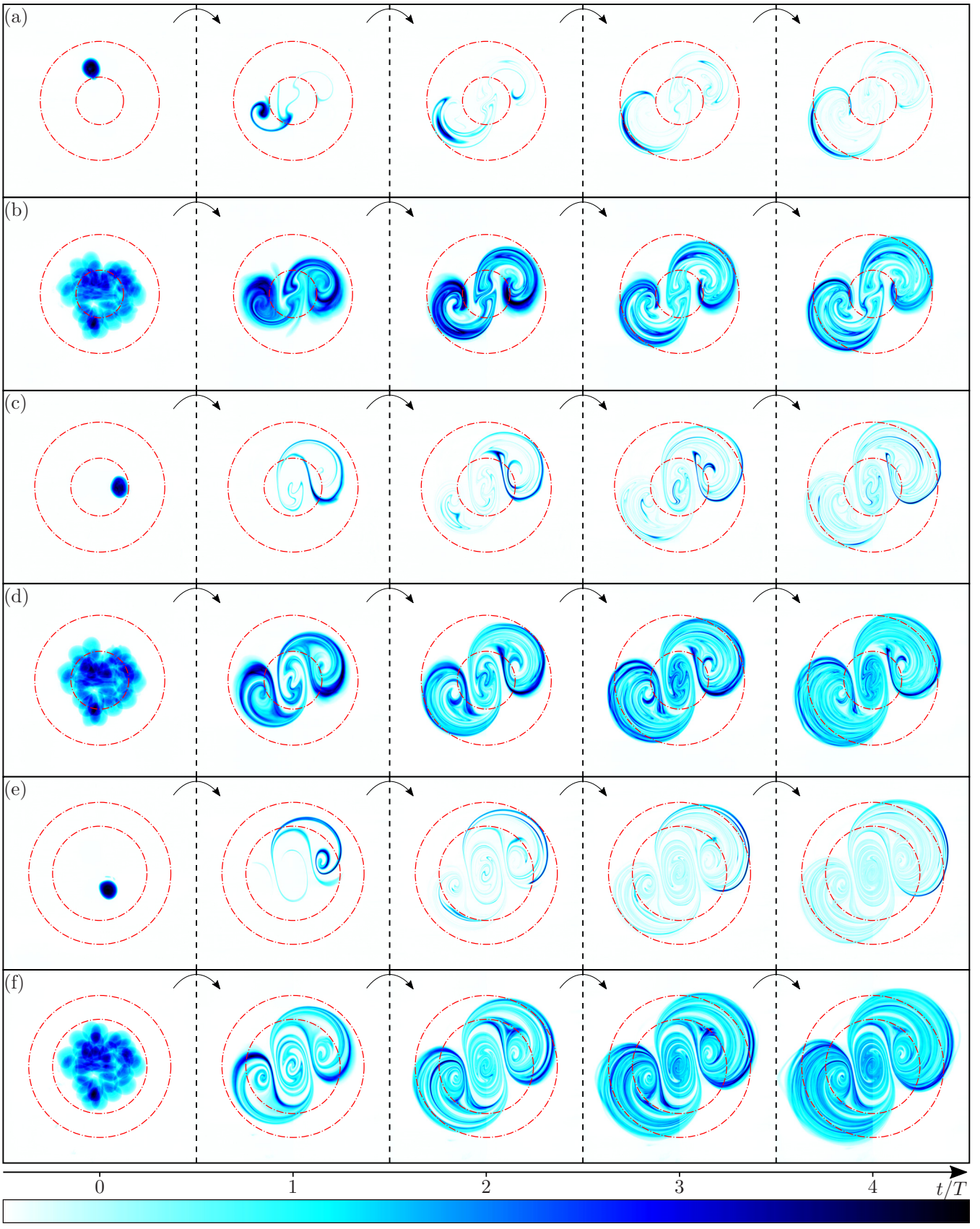

FIG. 8. Snapshots of the scalar patterns produced by the flows with T: (a), (b) 50 s; (c), (d) 100 s; and (e), (f) 200 s at $t/T \in [0,4]$. One arbitrary (a), (c), (e) and the combined initial condition (b), (d), (f) are presented. Extensional and mixing areas delimited. Palette ranges from 0 to max(θ).

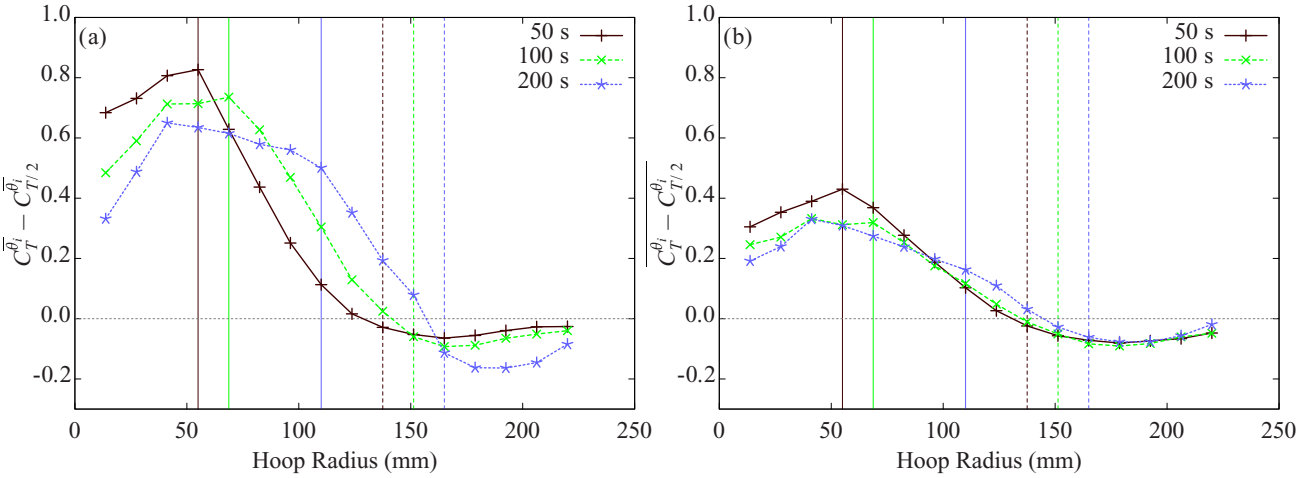

FIG. 9. Sizing of mixing area. Temporal average over the next-to-last cycle of the difference between the scalar correlation one period and half a period apart in different hoops. (a) Correlation of the sample average, $C_T^{\overline{\theta_i}} - C_{T/2}^{\overline{\theta_i}}$. (b) Average of the sample correlation, $\overline{C_T^{\theta_i} - C_{T/2}^{\theta_i}}$. In both graphs, vertical colored lines delimit the largest hoop fully embedded in the mixing area (solid lines) and the smallest hoop not containing any mixing area (dashed lines).

and two time instances (rows). In each configuration the size of the domain displayed is equal to the radius of the outer ring, summarized in Table I. This figure presents visual evidence of the scalar field convergence at times several periods apart and for different configurations at the same time. The large-scale scalar patterns are constant and consist of an increasing number of packed attenuated scalar layers with the number of cycles. In spite of the temporal and intersample recurrent shape cast by clean and dyed fluid, the distribution of the concentration varies among the different snapshots. This effect, contributing to reducing $\overline{C_T^{\theta_i}}$, is due to the long time scale of the extensional region, T_S, feeding the mixing area: Any inhomogeneity in the extensional region persists in the mixing area until it is completely homogenized by it at $t \gg T_S$.

The convergence of the scalar patterns is quantified through the average of the correlation between samples, presented in Fig. 12. To obtain that average, at each time step, each sample, i, was correlated with the rest, obtaining a total number of independent correlations to an average of $\binom{31}{2} = 465$. Figure 12 also presents the average of the correlation of each sample with the combined initial condition, presented in Fig. 2(b), obtained by virtue of the linearity of the transport operator. As in the one period correlation case, the correlations were performed in each case in a disk with a radius equal to the inner ring summarized in Table I and presented in Figs. 7 to 11, therefore containing only a mixing region, and using several length scales, $\mathcal{L}$.

Figure 12(a) presents the average correlation between the 465 pairs of samples (referred to hereafter as simple correlation) and the average correlation of the 31 different samples with the combined initial condition (referred to hereafter as combined correlation) as a function of t/T and for the minimum length scale considered, 1 pix $\approx$ 0.21 mm. This average correlation, which also contains the oscillatory

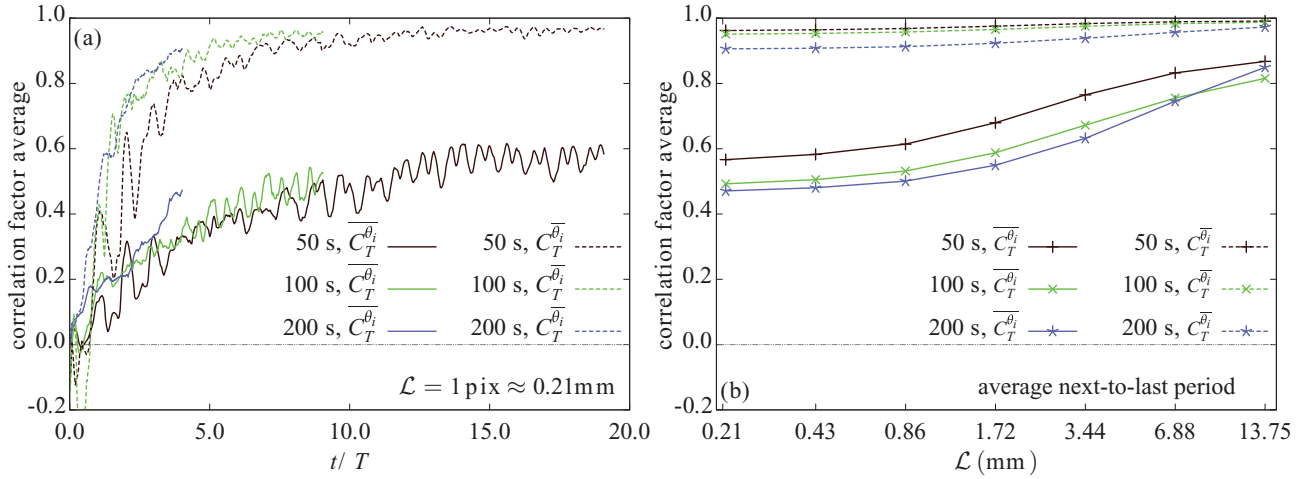

FIG. 10. Correlations between samples one period apart using the average of simple initial conditions, $\overline{C_T^{\theta_i}}$, and the combined initial condition, $C_T^{\overline{\theta_i}}$, presented against (a) the number of cycles and (b) the length scale, $\mathcal{L}$, of the correlation.

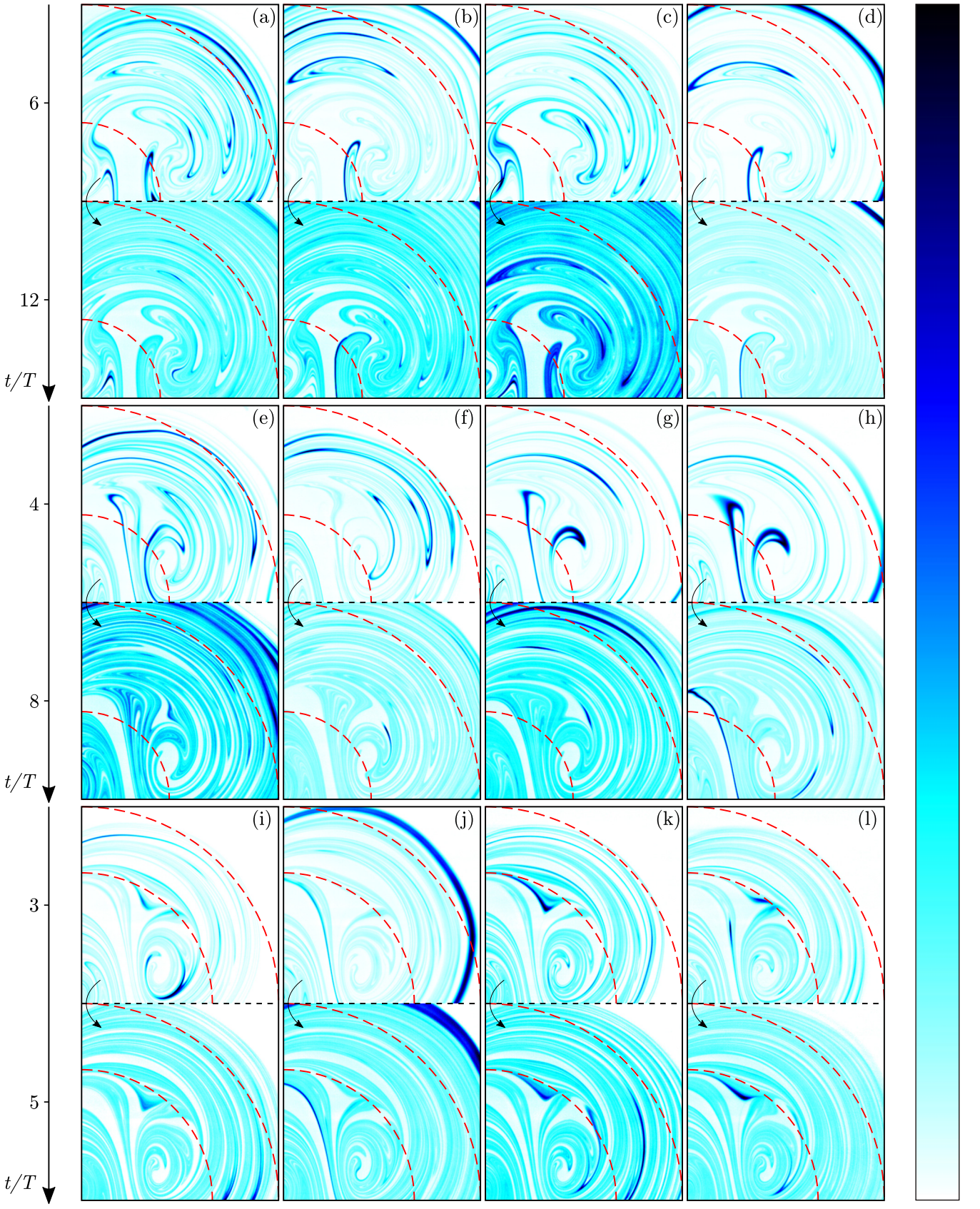

FIG. 11. Scalar patterns in the mixing area produced by flows with T: (a)–(d) 50 s; (e)–(h) 100 s; and (i)–(l) 200 s to different initial conditions at times t/T. Extensional and mixing areas delimited. Domains adjusted in each case to the outer ring in Table I. Palette ranges from 0 to max(θ).

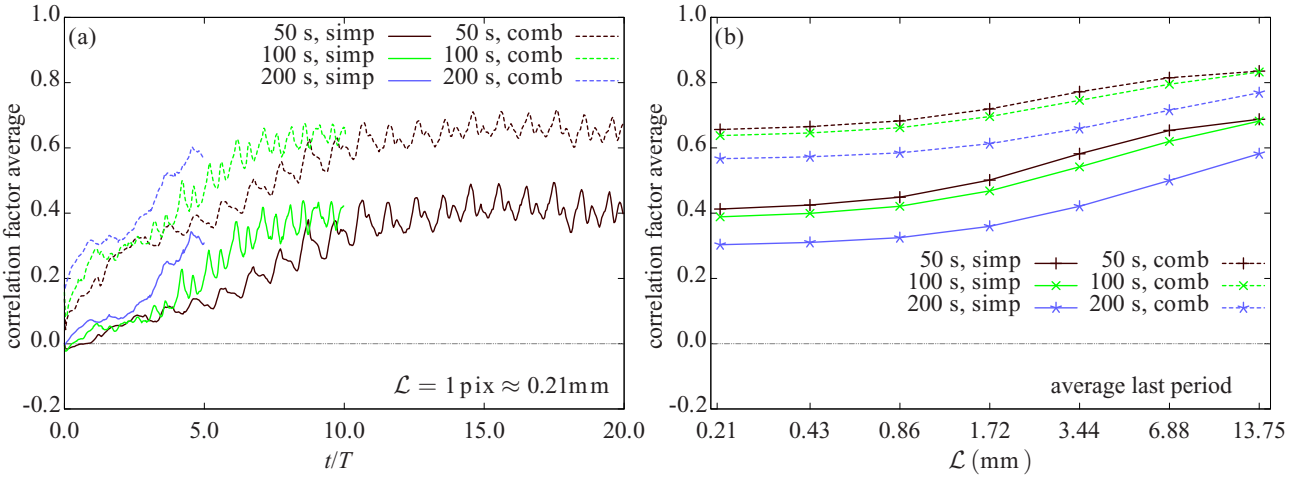

FIG. 12. Average of correlations intersample (simp) and with a combined initial condition (comb) presented against (a) the number of cycles and (b) the length scale of the correlation.

imprint of the cyclic forcing, is initially approximately 0 for the simple correlation and nearly 0 for the combined correlation cases $T = 50$ s and $T = 100$ s. The combined correlation in the case $T = 200$ s has an initial value of just under 0.2. The initial divergence from 0 of the combined correlation is due to the inhomogeneous distribution of initial conditions, which results in a higher correlation the larger is the area considered. For all cases the correlation increases with t/T, as the scalar patterns of the initial conditions align with the *global strange eigenmode*. After an initial transient, the average correlation seems to saturate at about 0.4 for the simple correlation and just above 0.6 for the combined correlation, for the flow periods $T = 50$ s and $T = 100$ s. The number of cycles completed for this saturation seems to decrease with T. Based on these observations, the case $T = 200$ s seems about to reach saturation. In the simple intersample average correlation, the maximum value obtained is around 80% of that value reached by $\overline{C_T^{\theta_i}}$ when $C_T^{\overline{\theta_i}} \sim 1$. Again, a low SNR and, especially, a more accused effect of the discrepancies of the inhomogeneities between different initial conditions in the extensional region feeding the mixing area at $t/T_S \ll 1$, were identified as the main reason for this mild correlation. Such inhomogeneity discrepancies in the extensional region between different initial conditions, and their impact on scalar distribution in the mixing region, can be qualitatively observed in Fig. 11. Still, the simple correlation presents a large scalar coherence in comparison with $\overline{C_{T/2}^{\theta_i}}$ and $C_{T/2}^{\overline{\theta_i}}$. The combined correlation which, by increasing the SNR and homogeneity of the extensional region in one of the fields, saturates at a larger value, demonstrates how the scalar pattern convergence is also independent on the scalar initial length scale. Figure 12(b) shows how the correlations presented in Fig. 12(a) nearly reach a flat slope at the minimum length scale considered and the resolution of the camera employed is sufficient to account for the minimum scalar length scales reached in the experiment.

A summary of the temporal evolution of the mixing statistics is presented in Fig. 13. Data are plotted until the dye in one of the samples leaves the camera area (CAM).

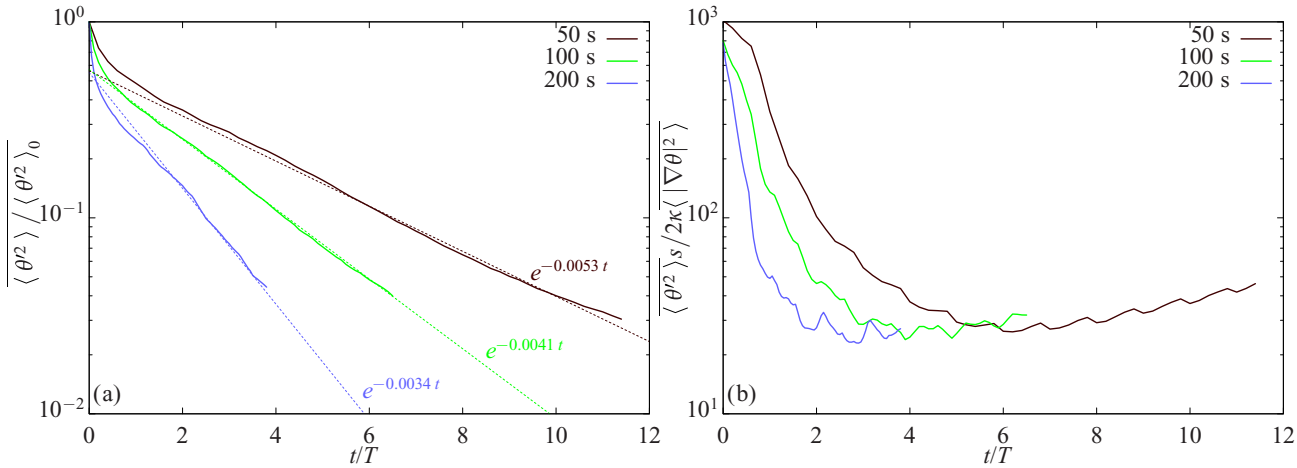

FIG. 13. Scalar statistics. (a) Temporal evolution of scalar variance and (b) mean gradient squared corrected with instantaneous scalar variance for the scalar advected by the unsteady flows.

Figure 13(a) presents the average variance decay. As expected for chaotic flows under the presence of the *strange eigenmode*, this variance decay is exponential, $\langle\theta'^2\rangle \propto e^{-st}$, for the three configurations. In such a regime, a constant ratio between variance and mean gradient squared should be expected, according to

$$\frac{d\langle\theta'^2\rangle}{dt} = -2\kappa\langle|\nabla\theta|^2\rangle. \tag{2}$$

Equation (2) was obtained by integrating Eq. (1) in a divergence-free flow using impermeable boundary conditions. The ratio between variance and mean gradient squared is presented in Fig. 13 (b) normalized with $s/2\kappa$. As observed, this ratio initially decreases and, coinciding with the variance exponential regime, reaches a plateau. As the variance keeps diminishing, the plateau slightly deviates from a constant value, likely due to the noise floor in the scalar measurements. Based on Eq. (2), the plateaus for all the forcing configurations presented in Fig. 13(b) should be equal to 1. However, even if the value of these plateaus are similar throughout the three flows, they are about 30 times larger than expected. This discrepancy is attributed to 3D effects, such as vertical velocity gradients, which increase the effective 2D diffusivity observed in the scalar [33,36]. If an effective diffusivity based on this corrected value, $\kappa_{\text{eff}} \approx 30\kappa$, was defined [33], the Péclet number characterizing these 2D experiments would still be $\text{Pe}_L^{2D} = U_{\text{rms}}L/\kappa_{\text{eff}} \approx 10^5 \gg 1$, as required in order to observe the *strange eigenmode*.

IV. CONCLUSIONS

The convergence towards a common scalar shape, independent of the scalar initial condition, of a scalar mixed by chaotic advection, was qualitatively and quantitatively evidenced. This is a cornerstone of the eigenmode description of chaotic mixing [2,3,8,13,14], which is based on the existence of a unique mode shape in each chaotic flow. Such a mode, strictly defined by the velocity field, is expected to govern the long-term scalar mixing statistics of any scalar used, regardless of its initial condition or scalar diffusivity. Evidence of a minimum length scale in the scalar patterns was also provided.

The flows employed for this experiment were inspired by the tendril-whorl map [24,25], which consists of a periodic switching between two concentric hyperbolic and elliptic stagnation points. The flows obtained exhibited the key kinematic features predicted in the theoretical analysis of the tendril-whorl map [25]. Among these features, the most remarkable were the clear separation between an external extensional and an internal mixing region, which increased in size with the flow period, and the characteristic conduits between these two, making a unique inhomogeneous chaotic zone. Some of those kinematic features imprinted characteristic shapes identifiable in the scalar patterns.

As expected in a chaotic mixer, the long-term variance decay of the scalar became exponential. The ratio between variance decay and mean gradient square was affected by 3D effects modifying the 2D diffusivity observed in the scalar, as explained in [33].

[1] A. Pikovsky and O. Popovych, Persistent patterns in deterministic mixing flows, Europhys. Lett. **61**, 625 (2003).

[2] D. R. Fereday, P. H. Haynes, A. Wonhas, and J. C. Vassilicos, Scalar variance decay in chaotic advection and Batchelor-regime turbulence, Phys. Rev. E **65**, 035301 (2002).

[3] A. Wonhas and J. C. Vassilicos, Mixing in fully chaotic flows, Phys. Rev. E **66**, 051205 (2002).

[4] J. D. Farmer, E. Ott, and J. A. Yorke, The dimension of chaotic attractors, Physica D (Amsterdam, Neth.) **7**, 153 (1983).

[5] V. I. Arnold, *Mathematical Methods of Classical Mechanics*, 2nd ed. (Springer-Verlag, Berlin, 1989).

[6] J. L. Thiffeault and S. Childress, Chaotic mixing in a torus map, Chaos **13**, 502 (2003).

[7] J. L. Thiffeault, C. R. Doering, and J. D. Gibbon, A found on mixing efficiency for the advection-diffusion equation, J. Fluid Mech. **521**, 105 (2004).

[8] J. L. Thiffeault, The strange eigenmode in lagrangian coordinates, Chaos **14**, 531 (2004).

[9] P. Haynes and J. Vanneste, What controls the decay of passive scalars in smooth flows? Phys. Fluids **17**, 097103 (2005).

[10] Y.-K. Tsang, T. M. Antonsen, Jr., and E. Ott, Exponential decay of chaotically advected passive scalars in the zero diffusivity limit, Phys. Rev. E **71**, 066301 (2005).

[11] T. M. Antonsen, Z. Fan, E. Ott, and E. Garcia-Lopez, The role of chaotic orbits in the determination of power spectra of passive scalars, Phys. Fluids **8**, 3094 (1996).

[12] G. K. Batchelor, The effect of homogeneous turbulence on material lines and surfaces, Proc. R. Soc. London, Ser. A **213**, 349 (1952).

[13] W. Liu and G. Haller, Strange eigenmodes and decay of variance in the mixing of diffusive tracers, Physica D (Amsterdam, Neth.) **188**, 1 (2004).

[14] R. T. Pierrehumbert, Tracer microscale in the large-eddy dominated regime, Chaos, Solitons Fractals **4**, 1091 (1994).

[15] R. T. Pierrehumbert, Lattice models of advection-diffusion, Chaos **10**, 61 (1999).

[16] D. Rothstein, E. Henry, and J. P. Gollub, Persistent patterns in transient chaotic fluid mixing, Nature (London) **401**, 770 (1999).

[17] M. C. Jullien, P. Castiglione, and P. Tabeling, Experimental Observation of Batchelor Dispersion of Passive Tracers, Phys. Rev. Lett. **85**, 3636 (2000).

[18] G. A. Voth, G. Haller, and J. P. Gollub, Experimental Measurements of Stretching Fields in Fluid Mixing, Phys. Rev. Lett. **88**, 254501 (2002).

[19] M. C. Jullien, Dispersion of passive tracers in the direct enstrophy cascade: Experimental observations, Phys. Fluids **15**, 2228 (2003).

[20] G. A. Voth, T. C. Saint, G. Dobler, and J. P. Gollub, Mixing rates and symmetry breaking in two-dimensional chaotic flow, Phys. Fluids **15**, 2560 (2003).

[21] E. Gouillart, O. Dauchot, J. L. Thiffeault, and S. Roux, Open-flow mixing: Experimental evidence for strange eigenmodes, Phys. Fluids **21**, 023603 (2009).

[22] E. Gouillart, O. Dauchot, and J. L. Thiffeault, Measures of mixing quality in open flows with chaotic advection, Phys. Fluids **23**, 013604 (2011).

[23] W. L. Chien, H. Rising, and J. M. Ottino, Laminar mixing and chaotic mixing in several cavity flows, J. Fluid Mech. **170**, 355 (1986).
[24] M. V. Berry, N. L. Balazs, M. Tabor, and A. Voros, Quantum maps, Ann. Phys. **122**, 26 (1979).
[25] D. V. Khakhar, H. Rising, and J. M. Ottino, Analysis of chaotic mixing in two model systems, J. Fluid Mech. **172**, 419 (1986).
[26] P. Tabeling, S. Burkhart, O. Cardoso, and H. Willaime, Experimental Study of Freely Decaying Two-Dimensional Turbulence, Phys. Rev. Lett. **67**, 3772 (1991).
[27] L. Rossi, S. Bocquet, S. Ferrari, J. M. Garcia de la Cruz, and S. Lardeau, Control of flow geometry using electromagnetic body forcing, Int. J. Heat Fluid Flow **30**, 505 (2009).
[28] W. H. Press, S. A. Teukolsky, W. T. Vetterling, and B. P. Flannery, *Numerical Recipes in C: The Art of Scientific Computing*, 2nd ed. (Cambridge University Press, Cambridge, U.K., 1995).
[29] J. M. Garcia de la Cruz, Experimental study of free surface mixing in vortical and chaotic flows, Ph.D. thesis, Imperial College London, 2011.
[30] J. M. García de la Cruz, J. C. Vassilicos, and L. Rossi, Topologies of velocity-field stagnation points generated by a single pair of magnets in free-surface electromagnetic experiments, Phys. Rev. E **90**, 043001 (2014).
[31] J. F. Foss, Surface selections and topological constraint evaluations for flow field analyses, Exp. Fluids **37**, 883 (2004).
[32] G. G. Guilbault, *Practical Fluorescence*, 2nd ed. (Marcel Dekker, New York, 1973).
[33] J. M. Garcia de la Cruz, L. C. Rossi, and J. C. Vassilicos, Three-dimensional effects in quasi two-dimensional free surface scalar experiments, Exp. Fluids **55**, 1835 (2014).
[34] D. Axelrod, D. E. Koppel, J. Schlessinger, E. Elson, and W. W. Webb, Mobility measurement by analysis of fluorescence photobleaching recovery kinetics, Biophys. J. **16**, 1055 (1976).
[35] N. T. Ouellette and J. P. Gollub, Dynamic topology in spatiotemporal chaos, Phys. Fluids **20**, 064104 (2008).
[36] B. S. Williams, D. Marteau, and J. P. Gollub, Mixing of a passive scalar in magnetically forced two-dimensional turbulence, Phys. Fluids **9**, 2061 (1997).